RESEARCH PAPER



Data-driven metamaterial design with Laplace-Beltrami spectrum as "shape-DNA"

Liwei Wang 1,2 · Yu-Chin Chan 2 · Zhao Liu 3 · Ping Zhu 1 · Wei Chen 2 10

Received: 17 September 2019 / Revised: 26 December 2019 / Accepted: 24 January 2020 / Published online: 19 February 2020 © Springer-Verlag GmbH Germany, part of Springer Nature 2020

Abstract

The design of multiscale metamaterial systems often suffers from high computational cost and incompatible boundaries between unit cells. As a result, unit cells are either assumed to be repeated (periodic) everywhere or limited to a small number of shapes. To address these limitations, this work proposes a data-driven design framework consisting of a metamaterial genome with a reduced-order geometrical representation as well as methods for the efficient design and analysis of 2D aperiodic metamaterials with compatible boundaries. To collect a large amount of designs, a set of unit cells generated by topology optimization is taken as initial seeds for the genome, and then expanded iteratively through random shape perturbations to form a rich database that covers a wide range of properties. For a reduced-order representation, the Laplace-Beltrami (LB) spectrum is adopted to describe complex unit cell shapes using a low number of descriptors, therefore significantly reducing the design dimensionality. Moreover, the physical and geometrical information contained in the LB spectrum is revealed through both quantitative and theoretical analysis. This information as well as the lower dimensionality allows the genome to be effectively leveraged to build a neural network model of structure-property relations for the rapid design of new unit cells. Finally, the combination of the metamaterial genome with an efficient optimization method based on the Markov random field (MRF) model is proposed to ensure connected boundaries between unit cells in multiscale aperiodic microstructure designs.

 $\textbf{Keywords} \ \ Data-driven \ design \cdot Metamaterials \cdot Boundary \ connectivity \cdot Microstructure \cdot Multiscale \ design \cdot Laplace-Beltrami \ spectrum$

1 Introduction

Metamaterials are man-made materials that achieve unusual properties through the design of the geometry of microstructures rather than material compositions (Zheludev 2010). They have gained much attention in recent years for their

Responsible Editor: Mehmet Polat Saka

- ☐ Ping Zhu pzhu@sjtu.edu.cn
- Wei Chen weichen@northwestern.edu
- The State key laboratory of Mechanical System and Vibration, Shanghai Key Laboratory of Digital Manufacture for Thin-walled Structures, School of Mechanical Engineering, Shanghai Jiao Tong University, Shanghai 200240, People's Republic of China
- Department of Mechanical Engineering, Northwestern University, 2145 Sheridan RD Tech B224, Evanston, IL 60201, USA
- School of Design, Shanghai Jiao Tong University, Shanghai 200240, People's Republic of China

superior and even counter-intuitive properties, enabling higher tunability of properties in structural design (Yu et al. 2017). Although metamaterials ignite the possibility of obtaining spatially varying properties for multiple functions, designing the full structure becomes a rather complex two-scale problem. At the macro-scale, the spatial distribution of materials and properties is optimized to meet multiple design performance targets, while at the micro-scale, each unit cell, or microstructure, needs to be designed for specific properties at different locations.

For design at the micro-scale, various topology optimization (TO) methods have been developed to achieve desired properties, including the density-based solid isotropic material with penalization (SIMP) method (Sigmund 1994; Xia and Breitkopf 2015), the level set-based method (LSM) (Wang et al. 2014)', and the evolutionary structural optimization method (ESO) (Huang et al. 2011). However, these computational design methods mainly focus on extreme properties rather than tunable properties over a wide range. When designing for high-dimensional target properties, different initial designs tend to drive the optimization process to different



local optima and may even fail to generate a practical structure. Furthermore, there is no strict bound for the competing effective properties of free-form unit cells (Cadman et al. 2012), leaving insufficient information on the attainable material properties for the metamaterials design. The key challenge here is that metamaterial design is an inverse problem without much a priori knowledge of the structures for target properties while the geometrical design space is infinite-dimensional.

For the design of full multiscale structures, most physics-driven methods adopt a "top-down" framework, tiling the shapes of microstructures according to their macroscopic loads (Kato et al. 2017; Rodrigues et al. 2002; Yan et al. 2014). These methods typically use homogenization theory to decouple the macro-scale design from a set of individual micro-scale designs. While this decoupling can accelerate the design process, the number of design variables is still large for a multiscale structure and computationally infeasible for practical designs. Moreover, since each cell is optimized separately, adjacent unit cells may not connect to each other, resulting in large deviations from target properties or manufacturing infeasible designs.

Several modifications have been made to address the connectivity issue, including adding fixed connectors (Deng and Chen 2017; Deng et al. 2019), pseudo loads, a nonlinear diffusion term (Zhou and Li 2008), and extra constraints (Du and Kim 2018) to the macro-scale optimization. While these modifications can relieve the connectivity issue to some extent, they either sacrifice the generality or do not scale well.

Recently, the data-driven approach is emerging as a promising answer to these challenges. Similar concepts reported in literature include digital materials (Hiller and Lipson 2009), building blocks (Mironov et al. 2009), unit cell library (Chu et al. 2008), elastic textures (Panetta et al. 2015), material library (Bickel et al. 2010), interpolating microstructures (Cramer et al. 2015), size-gradient unit cells (Han and Wen 2018), graded lattice materials/microstructures (Wang et al. 2017), and substructuring (Wu et al. 2019), to name a few. These methods use a similar "bottom-up" framework: generating a parameterized database of unit cells with similar shapes to assemble the full structure for spatially varying properties. While these methods can address the problem of connectivity and computation cost, they force configurations to be alike and require an elaborate process for data generation that often produces a limited set of properties, curbing the applicability of the database. To remedy the loss of generality, Schumacher et al. proposed to assemble a database with several families of metamaterials, enabling smoothly varying properties over a wide range by interpolation (Schumacher et al. 2015). They noted that different families would overlap in the multi-property space, providing various candidates for target properties. The best match can then be selected from those candidates for compatible boundaries. Since the design of material families is complex and may limit the variety of unit cells, Bo et al. established a larger and richer database by randomly adding and deleting elements in the voxelized unit cell (Bo et al. 2017; Chen et al. 2018). The unit cells can then be screened and mapped to specific mechanical properties of the full structure with a heuristic algorithm. However, without a proper mechanism for organization and management, the complex and diverse forms of shapes derived from the stochastic method make it infeasible to generate new unit cells by interpolation and impose extra difficulty to form well-connected boundaries.

To overcome these limitations, we propose in this work a new framework for the data-driven design of 2D freeform metamaterials. Unlike existing frameworks, two additions, i.e., extraction of shape descriptors and machine learning, are introduced for a higher level of management in data-driven design. Within this framework, we present an autonomous and efficient method to generate a large metamaterial database with versatile forms of unit cells and a wide range of properties. The highly diversified 2D unit cells are then encapsulated with a powerful shape descriptor, the Laplace-Beltrami (LB) spectrum. Since this descriptor is also known as "Shape-DNA" (Reuter et al. 2006), we correspondingly name our database indexed by the LB spectrum the "metamaterial genome." This work is the first attempt in the literature to relate the LB spectrum to mechanical properties through theoretical and statistical analyses. We reveal in this paper that the additional mathematical structure induced by the LB spectrum enables understanding of structure-property relations, rapid datadriven metamaterial design, and tiling of boundary compatible unit cells. With the similarity metrics provided by the LB spectrum, a rigorous and highly parallelizable assembling process for the full structure is realized, taking both geometrical and mechanics-based matching qualities into account. Altogether, our framework allows the efficient design of a full structure with both aperiodic unit cells and matching boundaries, while imposing no extra requirement in the unit cell data generation process.

A graphical overview of the data-driven metamaterial design framework is shown in Fig. 1. The proposed pipeline to generate a rich database is illustrated in Section 2, and in Section 3 we give a brief introduction to the LB spectrum that indexes the complex unit cells in the database with just a few descriptors. To justify that the LB spectrum can serve as a good geometrical representation, in Section 4 we show that it contains rich information on mechanical properties and serves as a metric for the similarity of shapes. With LB spectra as indices of the database, methods to efficiently generate new unit cells and assemble the full multiscale structure with optimized boundary connectivity are presented in Section 5. Finally, we draw the conclusion in Section 6.



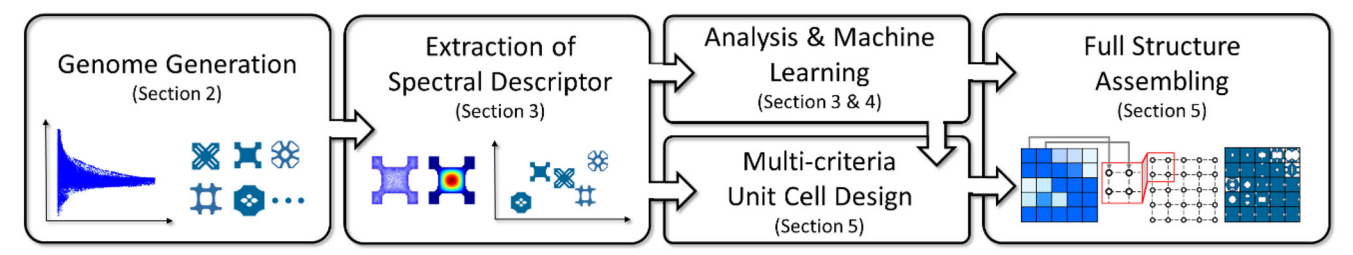


Fig. 1 Overview of the data-driven metamaterial design framework. The database is generated by perturbating the initial unit cell seeds sequentially. Unit cells in the database are mapped to a reduced-order spectrum space with their LB spectrum as coordinates. Through analysis, it is found that the characteristics of the spectrum provide a

higher level of management for the database, mimicking the function of DNA sequences. It enables rapid shape clustering, understanding of structure-property relations, data-driven metamaterial design of a full structure by an MRF model-based method through interpolation, and tiling with boundary compatible unit cells

2 Metamaterial genome generation

In data-driven design, a large database of precomputed unit cells whose data points are dense and cover a broad range of properties is desired. The former characteristic can provide numerous different candidates for a specific property, which can help to form compatible boundaries, while the latter enables greater freedom in the multiscale design. Given the shape of a unit cell, it is relatively easy to obtain its effective properties though homogenization (Andreassen and Andreasen 2014; Hassani and Hinton 1998). However, when generating a database from scratch, the geometry is not known and leads to the less straightforward inverse design problem of finding a unit cell with prescribed mechanical properties. To our best knowledge, no tight bound has been found for the achievable properties of unit cells (Cadman et al. 2012), which means that the target properties could fall in an infeasible and unattainable region. Moreover, a specific property can correspond to different unit cells, thereby making TO-based design sensitive to the initial guess.

To address these challenges, we propose a two-stage pipeline to efficiently construct a large unit cell database. We first generate an initial dataset by TO techniques such as SIMP and then proceed to populate the dataset iteratively through stochastic shape perturbation. The resulting database discloses a bound for achievable properties and enables efficient selection of well-connected unit cells.

2.1 Initial sampling in the property space

This study mainly focuses on three components of the stiffness tensor, E_{11} , E_{22} , and E_{12} , as the desired mechanical properties. As the bounds of the achievable property space are unknown a priori, a rectangular grid of 1000 target properties is obtained by sampling a unit hypercube[0, 1]³ at 10 levels along each dimension of the property space. The SIMP method is then utilized to search for the corresponding unit cells of each sampled target (Xia and Breitkopf 2015). Specifically, the unit cell is discretized into a 50×50 grid of finite elements.

Each element is assigned a density value $\rho_e \in [0, 1]$, with Young's modulus E_e defined as

$$E_{\rm e}(\rho_{\rm e}) = E_{\rm min} + \rho_e^p (E_0 - E_{\rm min}),$$
 (1)

where E_{min} is a small value (10⁻⁹ is adopted here) to prevent singularity of the stiffness matrix, E_0 is Young's modulus of the matrix material, and p is a factor used to penalize intermediate densities for an approximate 0–1 solution. Following asymptotic homogenization, the corresponding effective stiffness tensor E_{ijkl}^H can be expressed in the discretized form as

$$E_{ijkl}^{H} = \frac{1}{|Y|} \sum_{e=1}^{N} (u_e^{ij})^{T} K_e u_e^{kl},$$
 (2)

where |Y| is the area of the design domain, N is the number of elements (2500 in this case), $K_{\rm e}$ is the element stiffness matrix, and u_e^{ij} is the element displacement under the unit test strain fields ε_0^{ij} with a periodic boundary constraint. Therefore, the design problem is formulated as

$$\min_{\rho} : \left\| E_p^H(\rho) - E_t^H \right\|_2
\text{s.t.} : \mathbf{K} \mathbf{U}^{kl} = \mathbf{F}^{kl}, k, l = 1, ..., 3
\sum_{e=1}^{N} v_e \rho_e / |Y| \le \mathbf{V}
0 \le \rho_e \le 1, e = 1, ..., N,$$
(3)

where E_p^H and E_t^H are the vectorized forms of, respectively, the predicted and target properties, \mathbf{K} is the global stiffness matrix, \mathbf{U}^{kl} and \mathbf{F}^{kl} are the global displacement vector and the nodal force vectors under the corresponding unit strain tests, v_e is the element volume, and V is the volume limit of the unit cell. It should be noted that, for each target, different V values (0.3, 0.5, 0.9) are tried to obtain the most optimal unit cell. Using the method of moving asymptotes (MMA) as the optimization algorithm (Svanberg 1987), an initial database $S_{initial}$ with 358 valid structures is generated. The remaining 642 target points do not result in feasible unit cells, which is largely due to the sampling grid overlapping with theoretically infeasible regions, and SIMP failing to meet the targets



because of its sensitivity to the initial guess as well as the volume constraint. These demonstrate the limitation of the TO-based methods when little prior knowledge is available. The property space of this initial database is shown in Fig. 2, where Poisson's ratio E_{12}/E_{11} is shown instead of E_{12} for a better illustration.

2.2 Stochastic shape perturbation

As discovered in the sampling process, TO may require trial and error to find a unit cell that meets the target properties; using the approach to generate a dense database is often not affordable. Therefore, we propose to expand the initial database via an iterative stochastic shape perturbation algorithm. The notion behind this is that a small perturbation of the shape tends to induce a relatively small change in its properties. In the shape perturbation algorithm, we use a radial distortion model (Kroon 2009):

$$x_{new} = \begin{cases} x_c + \frac{r_{new}}{r_{old}} (x_{old} - x_c) & \text{if } r_{old} \le R_0 \\ x_{old} & \text{if } r_{old} > R_0 \end{cases}, \tag{4}$$

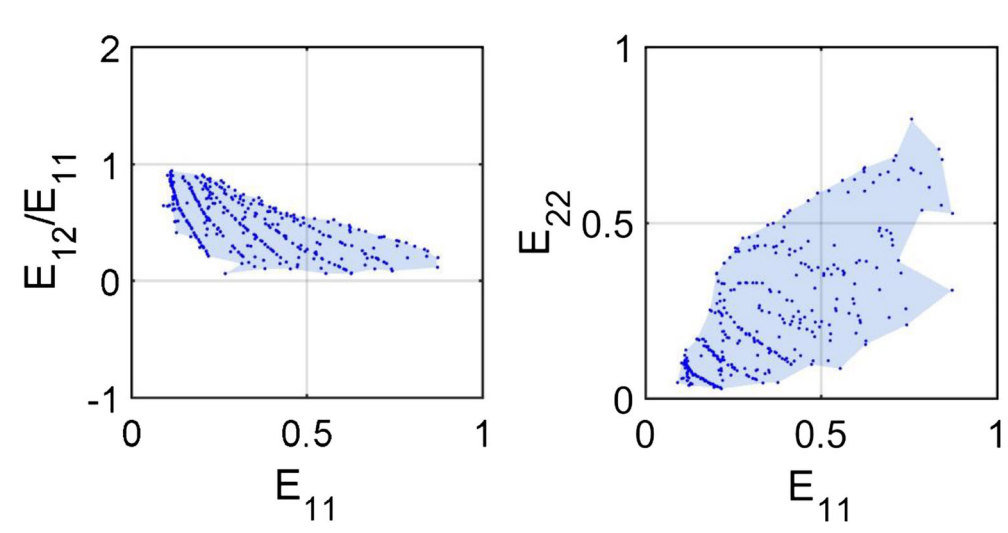
where x_{new} and x_{old} are the coordinates of the new and original pixel locations in the unit cell, x_{c} is the coordinate vector of the distortion center, r_{new} and r_{old} are the new and original distances to the distortion center, and R_0 is the radius of the distortion area. r_{new} is given as:

$$r_{new} = \begin{cases} \frac{1}{2} R_0 \left(1 - \cot\left(\frac{\gamma}{2}\right) - \beta\right) & \text{if } \gamma > 0\\ \frac{1}{2} R_0 \left(1 - \cot\left(\frac{\gamma}{2}\right) + \beta\right) & \text{if } \gamma < 0\\ r_{old} & \text{otherwise} \end{cases}$$
 (5)

where

$$\beta = \sqrt{\frac{2}{\sin^2(\gamma/2)} - \left(1 + \cot\left(\frac{\gamma}{2}\right) - \frac{2r_{old}}{R_0}\right)^2},\tag{6}$$

Fig. 2 The property space of the initial database with 358 structures, with shaded regions indicating the boundary of the property space



and $\gamma \in \left(-\frac{\pi}{2}, \frac{\pi}{2}\right)$ is the angle that controls the magnitude and direction of the distortion. A negative γ induces distortions towards the center, while a positive value enables distortions away from the center. As the absolute value of β becomes larger, the distortion will become greater. To preserve the orthogonal symmetry, we only feed a quarter of the original unit cell into the distortion model and then reassemble the full unit cell by duplication.

The distortion model in (4) has two attractive features: (i) Its parameters (R_0 , γ , and x_c) have clear interpretations, thus allowing easy implementation and tuning. To generate versatile forms of microstructures, these parameters are set as random variables with uniform distributions. (ii) It tends to preserve the structural integrity of unit cells and introduces negligible artifacts (e.g., disconnections and checkerboard patterns). Compared with the randomly assigned material distribution proposed by Bo et al., this perturbation method has a higher chance to generate feasible unit cells and is more efficient.

Several new unit cells generated by stochastic distortion are presented in Fig. 3.

It should be noted that disconnections may still appear in some extreme situations. Thus, to guarantee the feasibility of newly generated unit cells, morphological operations are used to fix small defects (i.e., isolated and spur pixels), and then to check the connectivity of the unit cells again. Unit cells with any unconnected features remaining are discarded. These tactics can be easily implemented using built-in morphological functions in MATLAB.

2.3 Iterative database expansion

With the stochastic shape perturbation algorithm, the initial database is then populated iteratively to achieve a denser and broader property space. During each iteration, the boundary of the current property space is approximated by a hull as



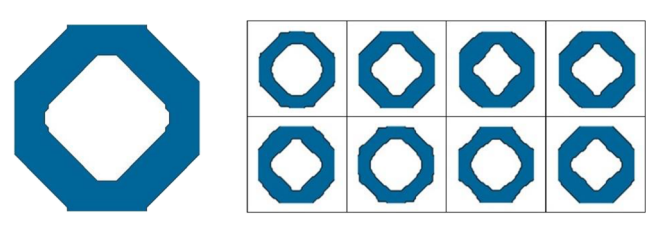


Fig. 3 The original unit cell (left) and unit cells generated by stochastic distortion

illustrated by the edge of the shaded regions in Fig. 2, enabling fast queries on whether a point is contained in the current property space. To do this, a 3D Cartesian grid is defined to enclose the current property space and each cell of this gird is assigned a binary value to indicate the outer/inner regions of the hull, forming a binary matrix. The L2 distance from the hull to each node of the Cartesian grid can then be calculated efficiently through the Euclidean distance transform of the binary matrix, and the L2 distance field can be estimated by linear interpolation within the grid.

With the approximated L2 distance field, the following score can be calculated for all existing unit cells:

$$Score = 1/[(d+\varepsilon)2^{\rho}],\tag{7}$$

where d is the L2 distance of each unit cell to the boundaries of the current property space, ρ is the number of data points inside a given radius in the property space (we recommend the radius to be 0.05 for more uniform sampling), and $\varepsilon \ll 1$ is used to avoid singularity. In each iteration, the 100 points with the highest scores are stochastically perturbed 20 times. Note that this selection method prefers points near the boundaries or in sparse regions. As the process goes on, the exponential term will dominate the numerator of score functions, thus enabling the algorithm to switch from exploration to exploitation. When the boundary of the property space no longer expands (i.e., $\Delta d < 0.1$) and the points inside the boundaries are relatively dense (average $\rho > 500$), the iterative process terminates. After removing duplicate microstructures, a dense

database, $S_{populated}$, of diverse shapes is obtained, expanding from 358 to 88,000 unit cells that cover a broader property space than the initial set from TO (see Fig. 2 vs. Fig. 4). The pseudo code of the algorithm is included in Table 6 in the appendix.

3 Unit cell characterization via spectral shape descriptors

In the metamaterials database, $S_{populated}$, the structure of each unit cell is stored in a 50×50 binary matrix. However, this pixel-based representation is high-dimensional, lacks physical interpretations, and does not have a simple metric to quantify the similarity in shapes. These drawbacks impose extra difficulty and complexity in data analysis and data-driven design. Therefore, it is advantageous to have a unified and reduced-order shape descriptor to represent all complex unit cells. In this section, the LB spectrum, also known as "Shape-DNA," is utilized to characterize the unit cells in $S_{populated}$. We introduce the LB descriptors and their calculation method in Sections 3.1 and 3.2, respectively, and then demonstrate their desirable characteristics using the descriptors of all unit cells in $S_{populated}$, thereby justifying the spectrum as an effective representation of the metamaterial genome.

3.1 An introduction to Laplace-Beltrami spectrum

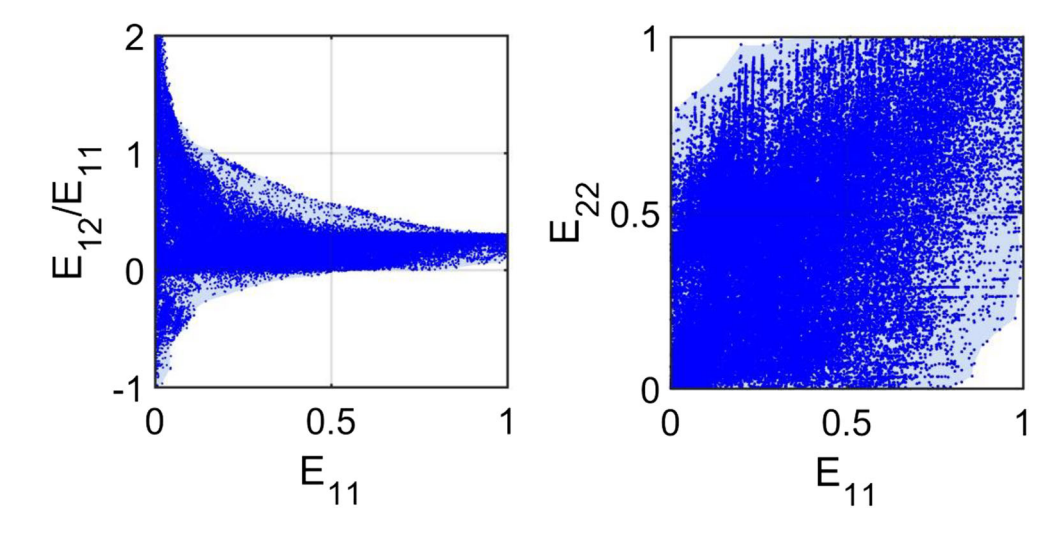
For a real-valued function f defined on a Riemannian manifold (Reuter et al. 2006), the Helmholtz equation is stated as:

$$\Delta f = -\lambda f,\tag{8}$$

where Δf is defined as:

$$\Delta f = div(grad \ f). \tag{9}$$

Fig. 4 The property space of the expanded database with 88,000 structures, with shaded regions indicating the boundary of the property space





The eigenvalues of the Helmholtz equation are named the LB spectrum and denoted:

$$0 \le \lambda_1 \le \lambda_2 \le \dots < \infty. \tag{10}$$

A 2D planar domain can be considered as a trivial case of Riemannian manifolds. In this case, the Helmholtz equation reduces to a Laplacian eigenvalue problem in a 2D Euclidean space. Under the Dirichlet boundary condition, this Laplacian eigenvalue problem can be formulated as

$$\frac{\partial^2 f}{\partial x^2} + \frac{\partial^2 f}{\partial y^2} = -\lambda f \text{ in } \Omega,$$

$$f = 0 \text{ on } \partial \Omega$$
(11)

where Ω and $\partial\Omega$ are the interior domain and corresponding boundaries, respectively.

LB spectrum has been widely used in the field of computer graphics for shape matching and classification, showing a powerful discrimination ability (Lian et al. 2013; Reuter et al. 2005). This fact provides confidence that the complex unit cells in the metamaterial genome can be well characterized by LB spectrum. Besides its powerful discrimination ability, LB descriptors also have some other attractive features (Lévy 2006; Reuter et al. 2006; Reuter et al. 2009); (i) The LB spectrum varies continuously with the shape of the planar domain, indicating that similar shapes have similar LB spectra. This feature provides a metric for similarity, which is desirable for data-driven analysis and design. (ii) Some useful geometrical information of the shape can be extracted from the spectrum, including perimeter, area, and Euler number. Because the physical properties of a unit cell are closely related to its shape, there are intrinsic but implicit relations between the LB spectrum and effective properties. Consequently, less training data and a much simpler model are needed to obtain an accurate model compared with voxel- or point-based representations. More details are provided in the following sections.

3.2 Numerical calculation method for LB spectrum

The eigenvalue problem in (11) can be written in its variational form by

$$a(f,\varphi) = \lambda b(f,\varphi) \text{ in } \Omega$$

$$f,\varphi = 0 \text{ on } \partial \Omega$$
 (12)

Fig. 5 Different stages in calculating the Laplace-Beltrami spectrum of a unit cell



$$a(f,\varphi) = \iint \nabla \varphi \cdot \nabla f d\Omega$$

$$b(f,\varphi) = \iint \varphi \cdot f d\Omega$$
(13)

The domain Ω is then divided into a triangular mesh with a linear shape function for each element. Thereby, f is approximated by

$$\widetilde{f}(x,y) = \sum_{i=1}^{M} F_i \Phi_i(x,y), \text{ with } F_i = f(P_i),$$
(14)

where F_i is the real value of f in nodal P_i , M is the total amount of triangular elements, and Φ_i is the linear nodal basis function (Su 2010). After substituting \widetilde{f} and Φ_i into φ and f, (14) can be transformed into its discretized form as

$$\sum_{i=1}^{M} F_i a(\Phi_i, \Phi_j) = \lambda \sum_{i=1}^{M} F_i b(\Phi_i, \Phi_j), \text{ for } j = 1, ..., M, (15)$$

which can be transformed into the matrix form to make it more compact:

$$AF = \lambda BF, \tag{16}$$

where

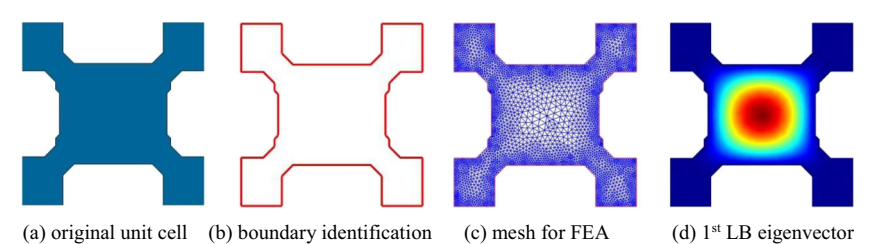
$$A_{ij} = \iint \nabla \Phi_j(x, y) \cdot \nabla \Phi_i(x, y) d\Omega B_{ij} = \iint \Phi_j(x, y) \cdot \Phi_i(x, y) d\Omega$$
(17)

It is straightforward to solve for the eigenvector F and the corresponding LB spectrum λ with direct solvers.

In our implementation, a L2 distance field is obtained for each unit cell, whose zero-level contour is extracted as the boundary. A triangular mesh is then constructed in the domain enclosed by the extracted boundary. After defining the Dirichlet boundary condition, the finite element model can be solved for the corresponding LB spectrum. An illustration for different stages in this process is given in Fig. 5.

3.3 The spectrum space of the database

The LB spectrum of each unit cell in the populated database, $S_{populated}$, is calculated by the finite element method above. The space spanned by the LB spectrum is defined to be the spectrum space of $S_{populated}$, and by indexing each unit cell with its LB spectrum, unit cells in $S_{populated}$ can be mapped





into a set of data points in the spectrum space. To select a proper dimension for the spectrum space, the minimal pairwise distance of each point is computed in the spectrum space spanned by 4, 8, 12, and 16 orders of LB spectrum, separately. Several representative quantiles of the minimal pairwise distance are computed to characterize the distribution, as shown in Table 1.

The minimal pairwise distance increases as the dimension of the spectrum space grows, which indicates that higher orders of LB spectrum can provide a greater discrimination ability. However, a high-dimensional spectrum space can also bring extra difficulties for data-driven methods. Therefore, the dimension should be kept as low as possible without sacrificing much discrimination power. As shown in Table 2, most points in a 16D spectrum space are located at least several units apart from each other. Meanwhile, a relatively small portion of point pairs have their mutual distance less than 0.1. These special pairs would not bring much trouble in practice since their shapes only differ by a few pixels and cause little change to the mechanical properties. Based on this observation, a 16D spectrum space is a proper compromise between discrimination power and complexity in our case.

For a better visualization of the pairwise distances, we map the 16D spectrum space to a 2D space using multidimensional scaling (MDS) (Borg and Groenen 1997). To demonstrate some important characteristics of the LB spectrum, some representative shapes are selected from $S_{populated}$ together with some artificial test shapes. These shapes are mapped into the 2D MDS plot shown in Fig. 6.

The MDS plot illustrates that the LB spectrum changes continuously if a shape transforms continuously (e.g., see the transformation of the unit cell with a single circular hole). In addition, similar shapes have similar LB spectra and may therefore be clustered in the spectrum space. This also means that the LB spectrum extracts some regular patterns from the shapes and embodies a metric for geometric similarity.

4 Quantitative analysis on spectrum-property relations

In this section, we delve more deeply into the physical information contained in the LB spectrum through both theoretical

and statistical analyses, providing the first connection between LB descriptors and mechanical properties in literature. Given the inherent information encoded by the LB spectrum, accurate neural network models can then be created as surrogates of the spectrum-property relation based on the metamaterial database, $S_{populated}$, which will tie into the later design step.

4.1 Physical information contained in the spectrum

4.1.1 Theoretical analysis

The LB spectrum and the homogenized properties are each derived from separate partial differential equations and boundary conditions, which renders the construction of an analytical relationship between spectrum and effective properties unlikely. However, since both LB spectrum and properties are calculated for the same shape, certain geometric quantities can be used as a bridge to link them. In fact, obtaining geometrical quantities in terms of the LB spectrum through asymptotic heat trace expansion has rigorous theoretical support from the area of shape analysis (Kac 1966; McKean and Singer 1967; Protter 1987). The key to this relation is that both the heat diffusion equation and the LB eigenvalue equation share the same differential operator, i.e., the LB operator, and are solved over the same shape, which in our study is the unit cell design.

Specifically, as shown by Reuter (Reuter et al. 2006), the heat trace technique can be used to approximate the area of a 2D shape with respect to the LB spectrum. In our case, the volume fraction of the unit cell is equal to the area of the unit cell normalized by the fixed design area (a square domain). Applying the heat trace expansion, we can estimate the volume fraction of the unit cell in terms of the LB spectrum as:

$$\upsilon \approx \frac{4\pi}{\lambda_{1}} \left[2\left(\sqrt{2}+2\right) \sum_{i=1}^{\infty} e^{-\frac{\lambda_{1}}{\lambda_{1}}} - \left(3\sqrt{2}+4\right) \sum_{i=1}^{\infty} 2e^{\frac{-2\lambda_{1}}{\lambda_{1}}} + \left(\sqrt{2}+1\right) \sum_{i=1}^{\infty} 4e^{-\frac{24}{\lambda_{1}}} \right]. \tag{18}$$

In addition, a rough range for the effective properties can be obtained by substituting the approximate volume fraction above into some estimated bounds, e.g., the Hashin-Shtrikman bounds shown below (Kachanov and Sevostianov 2018).

Table 1 Quantiles of the minimal pairwise distance in different dimensions from the dataset

Orders of LB	Lower sixteenths	Lower eighths	Lower fourths	Median	Upper fourths	Upper eighths	Upper sixteenths
4	7.52E-05	2.20E-03	0.02	0.18	0.57	1.52	3.30
8	3.69E - 04	1.10E - 02	0.12	0.90	2.83	7.92	17.25
12	1.07E - 03	0.03	0.38	2.17	6.34	16.84	36.01
16	2.65E - 03	0.07	0.84	3.97	10.79	27.37	57.01



Table 2	Correlation	anofficients between	I D cootrum	and mechanical properties	
rabie 2	Correlation	coefficients perween	LB spectrum	i and mechanical properties	

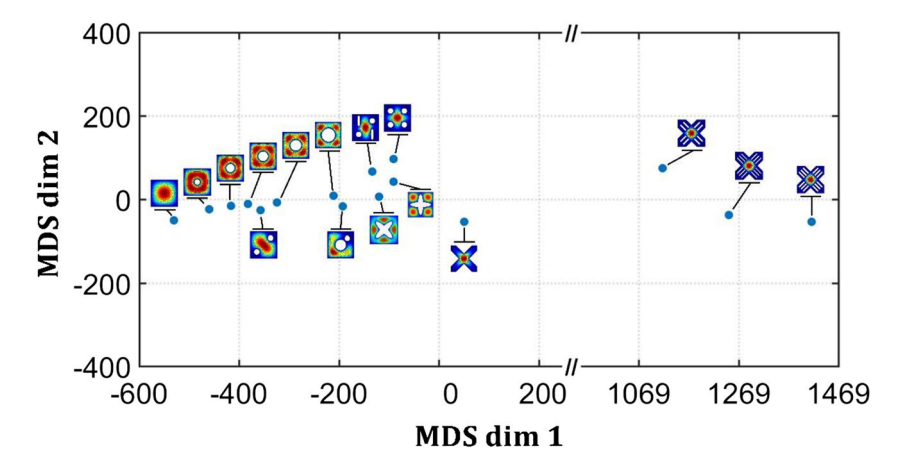
Order of LB	E11-LB correlation coefficients	E12-LB correlation coefficients	E22-LB correlation coefficients	Order of LB	E11-LB correlation coefficients	E12-LB correlation coefficients	E22-LB correlation coefficients
1	-0.59641	-0.30449	-0.41818	9	-0.69098	-0.41556	-0.49406
2	-0.64972	-0.36202	-0.45551	10	-0.68053	-0.41020	-0.48539
3	-0.67951	-0.39392	-0.49126	11	-0.68952	-0.41531	-0.49224
4	-0.67064	-0.39820	-0.47687	12	-0.68408	-0.41493	-0.48970
5	-0.68259	-0.40132	-0.48710	13	-0.68539	-0.41477	-0.48985
6	-0.66853	-0.39965	-0.47515	14	-0.67753	-0.40925	-0.48175
7	-0.68208	-0.40350	-0.48412	15	-0.68448	-0.41458	-0.48865
8	-0.68153	-0.40952	-0.48681	16	-0.68359	-0.41623	-0.48901

$$K_{HS}^{-} = 0, K_{HS}^{+} = K + \frac{\upsilon(\lambda_{i})}{-1/K + \frac{1 - \upsilon(\lambda_{i})}{K + \frac{4}{3}\mu}}$$
(19)

$$\mu_{HS}^{-} = 0, \mu_{HS}^{+} = \mu + \frac{\upsilon(\lambda_{i})}{-1/\mu + \frac{2[1 - \upsilon(\lambda_{i})](K + 2\mu)}{5\mu(K + \frac{4}{3}\mu)}},$$
(20)

where K and μ are bulk and shear moduli of the matrix material, $K_{\rm HS}^+(K_{\rm HS}^-)$ and $\mu_{\rm HS}^+(\mu_{\rm HS}^-)$ are Hashin-Shtrikman bounds for the unit cells. This suggests that the LB spectrum impacts the effective properties. Equations (18–20) also indicate that unit cells with larger LB spectrum values tend to have smaller volume fractions, and that the upper bounds of the effective elastic constants are expected to be lower as the spectrum increases. In turn, these relationships show that the LB spectrum encodes some physical information of the unit cell and is more than an abstract shape descriptor.

Fig. 6 A 2d multidimensional scaling plot of the 16D spectrum space of representative unit cells from the populated database and some artificial test shapes



4.1.2 Statistical analysis

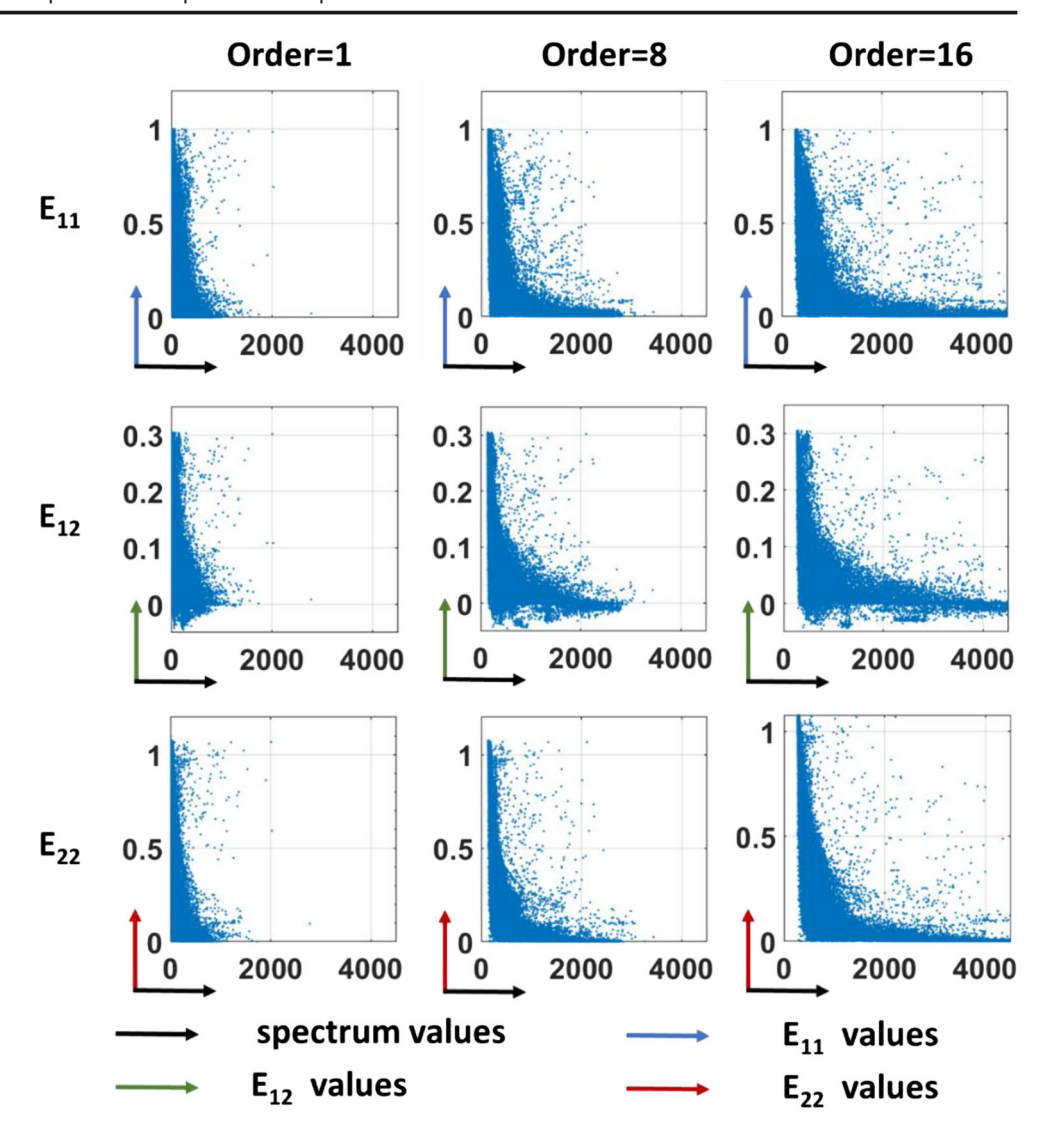
The previous theoretical analysis suggests a rough relation between the LB spectrum and effective mechanical properties. In this section, we carry out a statistical analysis on the populated database $S_{populated}$ to obtain further insight on the physical information contained in the spectrum.

To demonstrate the spectrum-property correlation, several representative scatter plots are drawn for selected orders of the LB spectrum and components of the stiffness tensor (E_{11} , E_{22} , and E_{12}) in Fig. 7.

Interestingly, these scatter plots exhibit similar L shapes, revealing a regular pattern on the relationship between the LB spectrum and different properties. The L-shaped pattern indicates that higher values in the LB spectrum correspond to a lower level and a narrower range of achievable mechanical properties. This is in good agreement with the analytical conclusion from the previous subsection.



Fig. 7 Scatter plots for 3 selected orders of LB spectrum and 3 components of the effective stiffness tensor



Correlation coefficients between LB spectrum values and mechanical properties can be further computed and shown in Table 2.

These coefficients lie within the range (-0.3, -0.7), indicating a clear negative correlation between LB spectrum and mechanical properties. This also confirms our previous theoretical prediction of the inverse relationship.

4.2 Surrogate modeling of structure-property relations with neural networks

After revealing the correlation between spectrum values and properties, their relation is further approximated by surrogate modeling, which reduces the complexity and computational cost in optimization. A two-layer feedforward-backpropagation neural network is adopted here because it provides great regression results for problems with nonlinear characteristics. The detailed structure of the network is given in Fig. 8.

The hyperparameters of this neural network are found through preliminary experiments. The neural network is fitted with the first 16 LB descriptors as inputs and the properties $(E_{11}, E_{22}, \text{ and } E_{12})$ as outputs. The dataset is randomly divided into a training set (60%), test set (20%), and validation set (20%) to prevent overfitting and underfitting. The result is shown in Table 3.

Fig. 8 Structure of the two-layer feedforward-backprop neural network

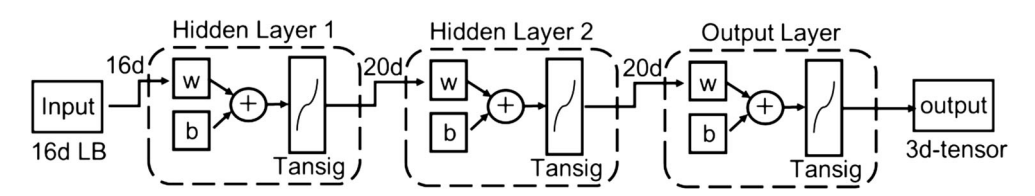




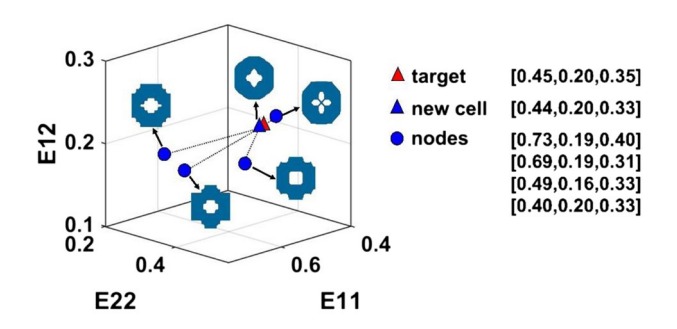
Table 3 MSE and R^2 values for the neural network

Target feature	Training set (60%)		Test set (20%)		Validation set (20%)	
	R^2	MSE	R^2	MSE	R^2	MSE
E11	0.96605	0.00429	0.96279	0.00448	0.96056	0.00467
E12	0.91900	0.00060	0.91716	0.00063	0.91316	0.00063
E22	0.91744	0.00666	0.90969	0.00732	0.91257	0.00694

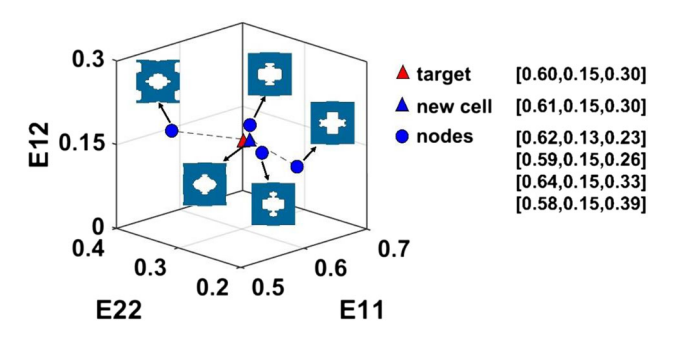
The neural network model has relatively high R^2 values and small mean squared errors (MSE), which is satisfactory considering the amount of data and the high nonlinearity of this problem. This accuracy can be partially attributed to the geometrical and physical information contained in the LB spectrum, distinguishing this spectrum descriptor from other high-ordered and abstract representations.

5 Design synthesis

Integrating all of the above methods into the proposed datadriven metamaterial design framework, we now demonstrate its benefits through two design scenarios. For the first, the collected genome and the created neural network model are used to design new unit cells with target stiffness tensor components. In the second, the genome is leveraged to design full



(a) example 1 for the interpolation process



(b) example 2 for the interpolation process

Fig. 9 New unit cells generated by interpolations. The results are visualized in the property space and the triplets in the legend correspond to $[E_{11}, E_{12}, E_{22}]$



multiscale aperiodic structures. To tackle the issue of boundary compatibility, we present an optimization method based on MRF graphs to select unit cells from groups of candidates with the same properties. Its efficacy is illustrated first using a hypothetical example with target properties assigned at different spatial locations, and finally through the design of cantilever beams with target displacement curves.

5.1 Data-driven unit cell design

Given a specific target property, one approach is to first try to retrieve the corresponding unit cells from the database, $S_{populated}$. However, there is a chance that $S_{populated}$ does not contain unit cells for all specified target properties. In this case, we propose to generate desirable unit cells by a two-step optimization scheme. In the first step, a heuristic optimization algorithm is applied to search for the optimal LB spectrum with the neural network. In the second step, new unit cells are generated from the optimal LB spectrum.

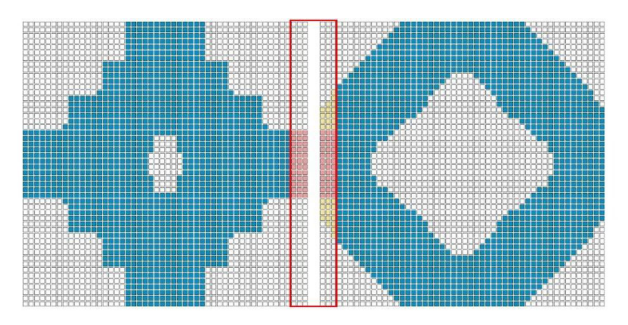
In Schumacher's work, a new unit cell with prescribed properties is generated by interpolating among points of a family with similar shapes and topology (Schumacher et al. 2015). However, for interpolation to work well, a database must be constructed by generating several families of unit cells with similar shapes, which limits the diversity of unit cells and complicates the micro-scale design process.

Instead, since the distance in the LB spectrum space can serve as a metric of the shape similarity, we divide existing data points in $S_{populated}$ near the target into several families by k-means clustering in the spectrum space. In this way, interpolation and data-driven unit cell design can be realized without imposing any extra constraints on the forms of unit cells when generating the database. In a selected cluster, we perform Delaunay triangulation in the property space, and take the vertices of the simplex containing our target as base unit cells for interpolation. We can then use the spectrum distance to instruct the interpolation weights by solving the following optimization problem:

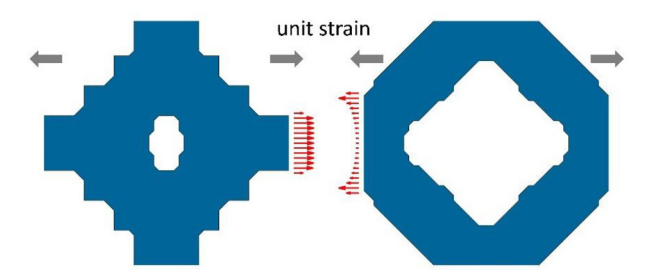
$$\min_{\mathbf{w}} \| \mathbf{E}^{t} - \mathbf{E}^{p}(\lambda) \|_{\infty \ S.t.} \ \lambda_{i-1} \le \lambda_{i}, \ \lambda_{i} = \sum_{j=1}^{k} w_{j} \widetilde{\lambda}_{ij}, \sum_{j=1}^{k} w_{j} = 1$$
 (21)

where E' and E'' are the vector forms of the target and predicted stiffness tensors, respectively. $\lambda = [\lambda_1, ..., \lambda_{16}]$ is the LB spectra of candidate unit cells for the target stiffness tensor,

Fig. 10 Illustration for geometrical pairwise energies θ^G_{ij} and mechanical pairwise energies θ^M_{ii}



(a) Illustration on geometrical pairwise energies θ_{ij}^G . The red bounding box defines the shared boundary area. θ_{ij}^G is the ratio of yellow elements over the sum of red and yellow elements.



(b) Illustration of the mechanical pairwise energies θ_{ij}^M . Red vectors are stresses on the shared boundary.

while λ_{ij} is the *i*th order LB spectrum value of the *j*th base unit cell. $\mathbf{w} = [w_1, ..., w_k]$ is the vector of weights of the *k* base unit cells. Genetic algorithm (GA) is adopted to search for the optimal weight distribution since it has advantages in multivariate and constrained problems, and the neural network of structure-property relations is used to expediently predict \mathbf{E}^p . After obtaining the optimal weights, the new structure is generated through linear interpolation of the distance fields of the base unit cells (Schumacher et al. 2015). Taking E_{11} , E_{22} , and E_{12} as design targets, two design examples for this method are shown in Fig. 9.

As shown in Fig. 9, the properties of newly designed unit cells are close to their respective design targets. Moreover, the base unit cells share similar shapes owing to the clustering on the spectrum space. This can help to reduce artifacts in the interpolated structure to guarantee the feasibility of the new design.

Although the interpolation method is efficient and easy to implement, there is a possibility that the interpolation might fail when the target falls outside every Delaunay simplex. In this situation, the optimal unit cell in each cluster can be taken

 Table 4
 Different sets of mechanical properties

	Set 1	Set 2	Set 3	Set 4	Set 5
E ₁₁	0.30	0.40	0.50	0.60	0.70
E_{12}	0.10	0.10	0.15	0.20	0.20
E ₂₂	0.30	0.40	0.50	0.60	0.70

as initial guesses for TO and then evolved to attain the target properties. Rather than using a random initial guess, this may provide faster convergence in TO as well as more diverse shapes for new designs.

5.2 Assembling the full multiscale structure with compatible boundaries

The incompatibility between adjacent unit cells in multiscale designs may deteriorate the mechanical properties and even make it infeasible to fabricate the full structure. Thus, to confront this critical challenge, we propose to form candidate groups via *k*-means clustering in the LB spectrum space, and then select from each group the unit cells that guarantee boundary compatibility while satisfying a spatially varying distribution of target properties.

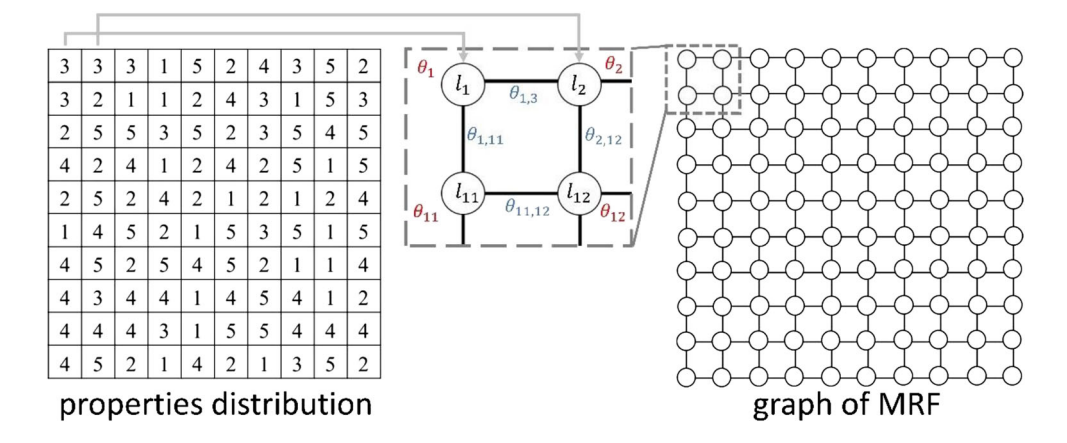
Before detailing the proposed design method, we first introduce the metrics with which we describe the suitability of candidate unit cells. To measure the match with respect to properties, the unitary energy is defined for each candidate as:

$$\theta_{\mathbf{i}}(l_{\mathbf{i}}) = \left\| \mathbf{E}^{t} - \mathbf{E}^{l_{i}} \right\|_{\infty}, \quad l_{\mathbf{i}} = 1, 2, \dots, k \tag{22}$$

where θ_i is the unitary energy for the *i*th cell, l_i is the label of the candidate building block assigned to the *i*th cell, k is the number of candidates assigned to each cell, and E^{l_i} is the elastic stiffness of the *i*th cell. If the properties of the selected building block are close to the target, the corresponding unitary energy should be small.



Fig. 11 The spatially varying properties distribution of a 10×10 square and the corresponding MRF graph. The number in each cell refers to the set of target properties in Table 5



As a second measure that quantifies the pairwise compatibility regarding boundaries, the pairwise energy between two neighboring structures is defined as:

$$\theta_{ij}(l_i, l_j) = \theta_{ij}^G(l_i, l_j) + \frac{1}{5}\theta_{ij}^M(l_i, l_j),$$
 (23)

where θ_{ij}^G is the percentage of incompatible pixels on the shared boundary of the material matrix (Du and Kim 2018), as shown in Fig. 10 a; θ_{ij}^M is the integration of the stress difference on the shared boundary divided by the sum of the stress under a unit strain field in the normal direction (Schumacher et al. 2015), as shown in Fig. 10 b. Note that θ_{ij}^M is set to be zero when the *i*th and *j*th cells are not adjacent or i = j.

If two neighboring structures are compatible both geometrically and mechanically, the corresponding pairwise energy value will be small. Therefore, finding the optimal combination of unit cells is equivalent to solving the following problem:

$$\min_{I} \sum_{i=1}^{n} \theta_{i}(l_{i}) + \sum_{i=1}^{n} \sum_{j>i}^{n} \theta_{ij}(l_{i}, l_{j}),$$
(24)

where $l = [l_1, ..., l_n]$ is the label assignment for n cells of the full structure. This discrete energy minimization problem is NP hard to solve. However, it can be interpreted as an inference problem on a grid-like MRF by taking each cell as a node (Wang et al. 2013), and then solved approximately but efficiently by the dual decomposition (DD-MRF) method (Komodakis et al. 2011).

Subsequently, our method is divided into the following three steps. Firstly, for each cell in the full structure, we select k different candidate designs either from the database, $S_{populated}$, or generated through our data-driven method (Section 5.1). To choose the most promising candidate groups from $S_{populated}$, we propose to perform k-means clustering in the LB spectrum space first and then select the most optimal unit cell in each cluster. This guarantees the diversity of the shapes, thus increasing the possibility of compatible boundaries between adjacent cells. Secondly, we assign the unitary and pairwise energies to the nodes and edges of the MRF, respectively. Finally, we optimize the combination of unit cells through DD-MRF, forming the full structure.

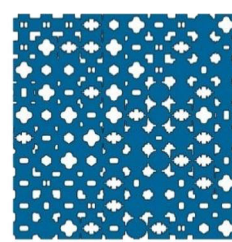
As an initial demonstration of the effectiveness of our method, we use a hypothetical example with 5 sets of properties randomly assigned to a 10×10 square macrostructure as shown in Table 4 and Fig. 11.

For each set of properties, four candidate groups are selected using different strategies: (i) 5 unit cells that best meet the target properties from $S_{populated}$ overall, (ii) 5 unit cells, one that best meets the target from each of 5 clusters in the LB spectrum space, (iii) 10 unit cells that best meet the target overall, and (iv) 10 unit cells, one that best meets the target from each of 10 clusters. DD-MRF is then used to find the optimized combination with different candidate groups. The optimized results are shown in Fig. 12 and Table 5.

For all groups regardless of selection strategy, the optimized adjacent unit cells connect to each other on the boundary while the deviation from the target properties at every location is small. Groups containing 10 candidates result in much lower energy values than those containing 5 candidates,

Fig. 12 The optimized combinations of unit cells for 4 different candidate groups









(a) candidate group 1

(b) candidate group 2

(c) candidate group 3

(d) candidate group 4



 Table 5
 Energies of the optimized combinations for 4 different candidate groups

	Group 1	Group 2	Group 3	Group 4
Unitary energy	1.41	1.90	1.56	2.32
Pairwise energy	54.61	50.68	45.96	38.45
Total energy	56.02	52.58	47.52	41.77

indicating a better-tiled boundary and properties distribution (Table 6). By selecting unit cells from different clusters, the optimized structure has better boundary compatibility and reaches a small deviation from the target properties. In fact, a larger candidate group together with more versatile forms of shapes provides a much larger design space, thus enabling a more optimal tiling combination.

We note that the DD-MRF optimization process converges quickly and takes only a few minutes to finish on a single CPU (Intel(R) Xeon(R) Gold 6144 CPU @3.50 GHz). Furthermore, DD-MRF decomposes the original problem into numerous simple sub-problems, making it amenable to parallel computation.

5.3 Cantilever beam examples

The procedure of structural synthesis is further applied to two cantilever beam examples for validation. As shown in Fig. 13, the design domain is a 40 mm \times 200 mm cantilever beam with the left end fixed and a vertical point force F=1 N at the center of the right end. The aim is to design a beam with aperiodic metamaterials unit cells that can achieve prescribed Y-displacement for the centerline of the beam. The target curves of Y-displacement versus the normalized length from different locations on the centerline to the left end of the beam are shown on the right plot of Fig. 13 for both examples. Note that the first example has a smoothly varying target displacement curve while the second has a sharp turning point in the

middle of the curve. In both cases, Young's modulus for the solid material is 1 MPa and Poisson's ratio is 0.3.

To study the influence of the size of the unit cell, the beam is discretized by 4×20 , 8×40 , and 16×80 grids for each example. A variable sheet thickness method (Sigmund et al. 2016) is adopted to decide the distribution of target properties in each cell of the grids first. The optimization objective for the sheet thickness method is defined as

$$f_{obj} = \frac{1}{N_{center}} \sum_{i=1}^{N_{center}} \left(v_i - \overline{v}_i \right)^2, \tag{25}$$

where N_{center} is the number of nodes located on the centerline while v_i and \overline{v}_i are the real Y-displacement and target Y-displacement for the *i*th node on the centerline respectively. Since the focus is the shape of the distorted beam, no volume restriction is applied here.

With the identified distribution of target properties, the proposed methods for the retrieval, generation, and assembling of unit cells can be used to map corresponding microstructures to each cell of the grids. In these two examples, 10 candidate unit cells are selected from different clusters in the LB spectrum space for each target property. Final designs are shown in Figs. 14 and 15.

These designs are performed on the aforementioned single CPU, with the execution time ranging from a few minutes to an hour, depending on the discretization. All designs have well-connected boundaries between unit cells despite different forms of topology. In the first example, the porosity is distributed evenly along the length of the beams to achieve a smooth displacement curve. Meanwhile, the beams in the second example have much higher porosity in the middle and at the location near the free end. This is because the target displacement consisting of two curves with different slopes will require different amount of stiffness. The left part with a smaller slope requires a stiffer material whilst the right part requires a less stiff one. From the resulting displacement curves, it can be

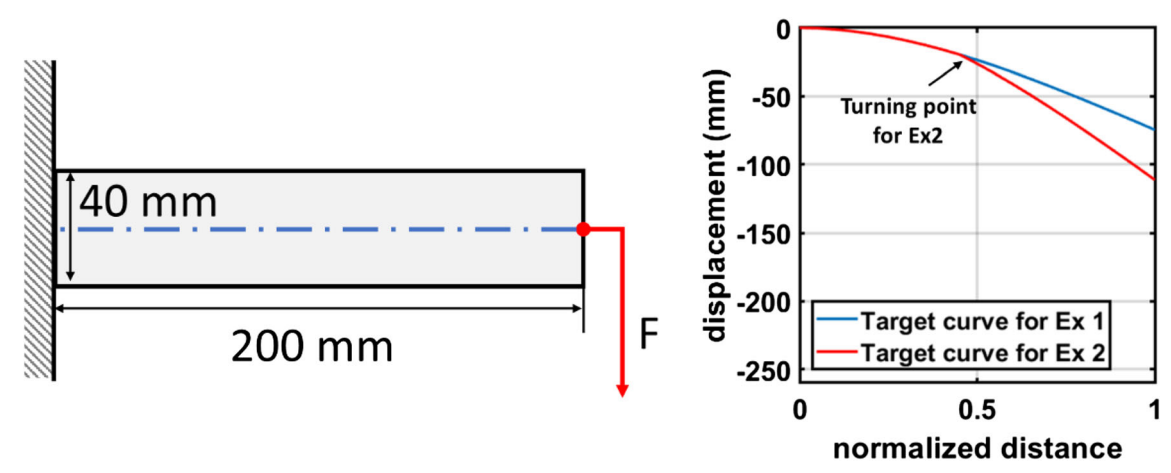
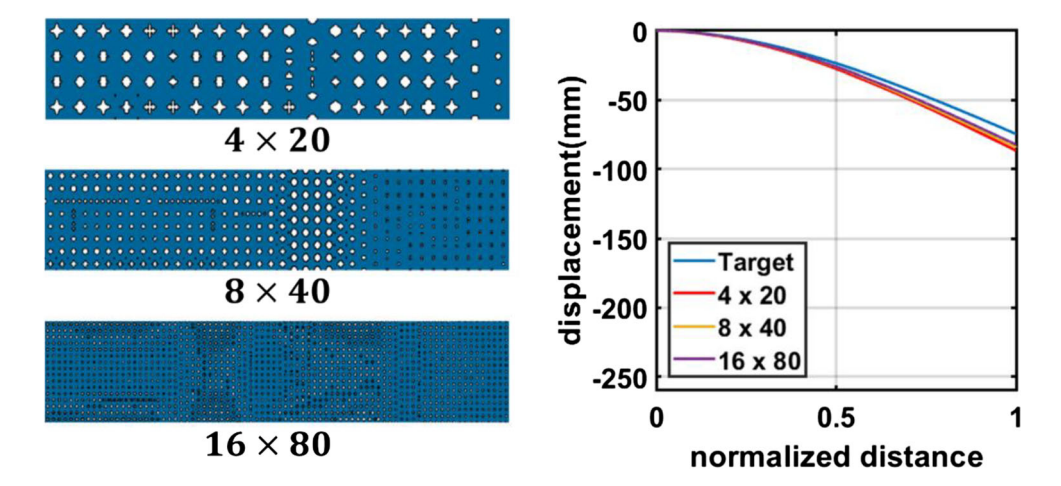


Fig. 13 The design domain and boundary conditions for the numerical example (left) and the target displacements (right)

Fig. 14 Beam designs (left) and displacements curves in the first example (right)



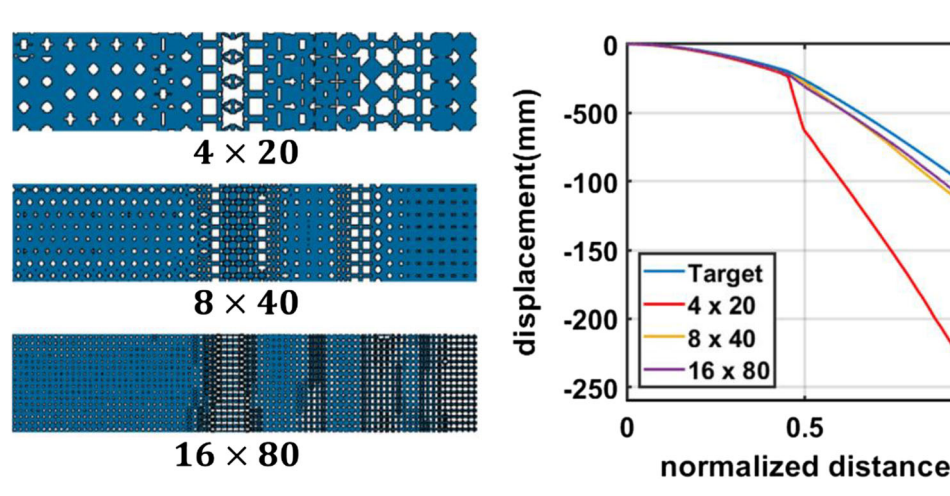
observed that designs with finer discretization can better match the target. The design with a 4×20 mesh in the second example exhibits a large deviation from the target, which is due to the failure of the size-separation hypothesis in the homogenization theory. All other curves achieve the displacement objectives with relatively small deviations.

Overall, a finer mesh together with a larger candidate group results in a better design, and our proposed framework performed well in designing a two-scale metamaterial system. Moreover, the appropriate shape changes induced by the abrupt turn in the second target displacement curve demonstrate the potential of this method to control deformation, nonlinear behavior, and performance such as mobility and induced buckling.

6 Conclusions

This study establishes a metamaterial genome with the LB spectrum as a shape descriptor that encapsulates and organizes highly diverse unit cells, enabling efficient generation of unit cell families, understanding of structure-property relationships, and data-driven metamaterial design and boundary compatible tiling.

Fig. 15 Beam designs (left) and displacements curves in the second example (right)



To provide greater freedom for design, a stochastic shape perturbation method is developed to obtain a metamaterials database covering a wide range of properties in an autonomous and efficient manner. Since this database, or genome, is large and contains very diverse unit cells, the commonly used pixel representation fails to provide effective data management. Therefore, a powerful spectral descriptor, the LB spectrum, is employed for the first time to represent unit cells in the genome with much-reduced dimension, allowing us to characterize unit cells with complex shapes using only 16 descriptors in the demonstrated cases. In addition, it is evident from our analysis that the LB spectrum contains rich physical information and provides an effective metric to differentiate between shape, benefitting the later design synthesis steps.

In the unit cell design, our neural networks, which act as surrogate models linking the spectrum to mechanical properties, provide satisfying prediction results as a direct result of the reduced dimension and the valuable physical information contained in the spectrum. By exploiting the LB spectrum as a metric for shape similarity, unit cell families can be easily discovered by clustering in the spectrum space and then used to interpolate new micro-scale designs.



To design a full macro-scale structure, we demonstrate that the boundary tiling challenge can be transformed into a grid-like MRF graph and then efficiently solved by the DD-MRF method. The results reveal that candidate groups with a greater number and variety of unit cells can enhance boundary compatibility, both of which can be easily achieved through clustering the dense and diverse genome in the spectrum space. Two examples of designing beams to achieve the desired spatially varying displacements further illustrate the potential of our methods. Compared with existing full structure assembly methods using a unit cell database, our method can provide better compatibility on the boundary without constricting the genome to pre-defined families of similar shapes.

The effectiveness of our data-driven approach utilizing a low dimensional LB spectrum representation is not limited to the relatively simple 2D problems shown in this work. In the computer graphics field, for example, the LB spectrum has been successfully employed for 3D geometries with a moderate increase of the dimension of the descriptors (Lévy 2006; Reuter et al. 2006). Research into extending our design framework to 3D, nonlinear, and multi-physics cases is underway. Another promising direction is to combine more advanced machine learning methods with the genome to design

structural systems with complex functionalities, such as pattern buckling, nonlinear deformation, and dynamic properties.

Acknowledgments The authors are grateful to Prof. K. Svanberg from the Royal Institute of Technology, Sweden, for providing a copy of the MMA code for metamaterial design.

Funding information The authors received financial support from the National Science Foundation (NSF) (grant no. OAC-1835782). Mr. Liwei Wang received financial support from Zhiyuan Honors Program for Graduate Students of Shanghai Jiao Tong University. Ms. Yu-Chin Chan also received financial support from the NSF Graduate Research Fellowship Program under grant no. DGE-1842165.

Compliance with ethical standards

Conflict of interest The authors declare that they have no conflict of interest.

Replication of results There are mainly 5 algorithms proposed in this paper: microstructure design, database extension, LB spectrum calculation, unit cell design, and DD-MRF for boundary optimization. Microstructure design is realized using the MATLAB code in (Xia and Breitkopf 2015) with minor modifications. Detailed pseudo code for database extension is given in Table 6 in the appendix. LB spectrum is calculated through the PDE toolbox in MATLAB. Detailed implementations of DD-MRF can be found in (Komodakis et al. 2011).

Appendix

Table 6 Pseudo code for populating the database

Algorithm 1 Procedure for populating the database iteratively

```
Procedure POPDATABASE (input: microstructures labeled with
          properties in initial database S_{initial}, output: microstructures labeled
           with properties in a populated database S_{populated})
               S_{populated} \leftarrow S_{initial}, \Delta d \leftarrow 1
2
               calculate \rho of each point in the property space of S_{populated}
3
               while \Delta d \ge 0.1 or mean(\rho) \le 500 do
                  compute the convex hull of the property space of S_{populated}
4
                  calculate the L2 distance d and \rho for the score function of each
5
                  point
                  select N = 100 unit cells with the highest score function values,
6
                  assign them to the set S_{seed} as the seeds for perturbation
7
                  for microstructure M_i in S_{seed}
8
                     i \leftarrow 0
9
                     while i < 20 do
10
                         M_i \leftarrow \text{perturbate } M_i \text{ and fix small defects}
11
                         if \widetilde{M}_i doesn't have unconnected components then
12
                            calculate the effective properties of \widetilde{M}_i
                            add \widetilde{\boldsymbol{M}}_{i} to \boldsymbol{S}_{populated}
13
14
                         end if
15
                         i=i++
16
                     end while
17
                  end for
18
                  calculate
19
               end while
              remove duplicate microstructures from S_{populated}
20
           end procedure
```



References

- Andreassen E, Andreasen CS (2014) How to determine composite material properties using numerical homogenization. Comput Mater Sci 83:488–495
- Bickel B, Bächer M, Otaduy MA, Lee HR, Pfister H, Gross M, Matusik W (2010) Design and fabrication of materials with desired deformation behavior. ACM Trans Graph 29:1. https://doi.org/10.1145/ 1778765.1778800
- Bo Z, Skouras M, Chen D, Matusik W (2017) Two-scale topology optimization with microstructures. ACM Trans Graph 36:164
- Borg I, Groenen P (1997) Modern multidimensional scaling: theory and applications modern multidimensional scaling: theory and applications New York, Berlin: springer-Verlag, 1997, xvii, 471 p ISBN 0387948457
- Cadman JE, Zhou S, Chen Y, Li Q (2012) On design of multi-functional microstructural materials. J Mater Sci 48:51–66. https://doi.org/10. 1007/s10853-012-6643-4
- Chen D, Skouras M, Bo Z, Matusik W (2018) Computational discovery of extremal microstructure families. Sci Adv 4:eaao7005
- Chu C, Graf G, Rosen DW (2008) Design for additive manufacturing of cellular structures. Computer-Aided Design Appli 5:686–696. https://doi.org/10.3722/cadaps.2008.686-696
- Cramer AD, Challis VJ, Roberts AP (2015) Microstructure interpolation for macroscopic design. Struct Multidiscip Optim 53:489–500. https://doi.org/10.1007/s00158-015-1344-7
- Deng J, Chen W (2017) Concurrent topology optimization of multiscale structures with multiple porous materials under random field loading uncertainty. Struct Multidiscip Optim 56:1–19
- Deng J, Pedersen CB, Chen W (2019) Connected morphable components-based multiscale topology optimization. Front Mech Eng 14:129–140
- Du Z, Kim HA (2018) Multiscale design considering microstructure connectivity. https://doi.org/10.2514/6.2018-1385
- Han Y, Wen FL (2018) A novel design method for nonuniform lattice structures based on topology optimization. J Mech Des 140:091403
- Hassani B, Hinton E (1998) A review of homogenization and topology opimization II—analytical and numerical solution of homogenization equations. Comput Struct 69:719–738
- Hiller J, Lipson H (2009) Design and analysis of digital materials for physical 3D voxel printing. Rapid Prototyp J 15:137–149
- Huang X, Radman A, Xie Y (2011) Topological design of microstructures of cellular materials for maximum bulk or shear modulus. Comput Mater Sci 50:1861–1870
- Kac M (1966) Can one hear the shape of a drum? Am Math Mon 73:1–23Kachanov M, Sevostianov I (2018) Micromechanics of materials, with applications vol 249. Springer, Berlin
- Kato J, Yachi D, Terada K, Kyoya T (2017) Micro-macro concurrent topology optimization for nonlinear solids with a decoupling multi-scale analysis. Int J Numer Methods Eng 113
- Komodakis N, Paragios N, Tziritas G (2011) MRF energy minimization and beyond via dual decomposition. IEEE Trans Pattern Anal Mach Intell 33:531–552
- Kroon D-J (2009) Pinch and spherize filter. https://www.mathworks.com/matlabcentral/fileexchange/22573-pinch-and-spherize-filter
- Lévy B Laplace-Beltrami eigenfunctions towards an algorithm that understands geometry. In: IEEE International Conference on Shape Modeling & Applications, 2006
- Lian Z et al (2013) A comparison of methods for non-rigid 3D shape retrieval. Pattern Recogn 46:449–461. https://doi.org/10.1016/j. patcog.2012.07.014
- McKean HP, Singer IM (1967) Curvature and the eigenvalues of the Laplacian. J Differ Geom 1:43–69

- Mironov V, Visconti RP, Kasyanov V, Forgacs G, Drake CJ, Markwald RR (2009) Organ printing: tissue spheroids as building blocks. Biomaterials 30:2164–2174. https://doi.org/10.1016/j.biomaterials. 2008.12.084
- Panetta J, Zhou Q, Malomo L, Pietroni N, Cignoni P, Zorin D (2015) Elastic textures for additive fabrication ACM. Transact Graphics 34(135):131–135:112. https://doi.org/10.1145/2766937
- Protter M (1987) Can one hear the shape of a drum? Revisited Siam Rev 29:185–197
- Reuter M, Wolter F-E, Peinecke N (2005) Laplace-spectra as fingerprints for shape matching. In: Proceedings of the 2005 ACM symposium on Solid and physical modeling. ACM, pp 101–106
- Reuter M, Wolter F-E, Peinecke N (2006) Laplace–Beltrami spectra as 'shape-DNA' of surfaces and solids. Comput Aided Des 38:342– 366. https://doi.org/10.1016/j.cad.2005.10.011
- Reuter M, Wolter FE, Shenton M, Niethammer M (2009) Laplace-Beltrami eigenvalues and topological features of eigenfunctions for statistical shape analysis. Comput Aided Des 41:739–755. https://doi.org/10.1016/j.cad.2009.02.007
- Rodrigues H, Guedes JM, Bendsoe MP (2002) Hierarchical optimization of material and structure. Struct Multidiscip Optim 24:1–10. https://doi.org/10.1007/s00158-002-0209-z
- Schumacher C, Bickel B, Rys J, Marschner S, Gross M (2015) Microstructures to control elasticity in 3D printing. ACM Trans Graph 34:136:131–136:113
- Sigmund O (1994) Materials with prescribed constitutive parameters: an inverse homogenization problem international. J Solids Struct 31: 2313–2329
- Sigmund O, Aage N, Andreassen E (2016) On the (non-) optimality of Michell structures. Struct Multidiscip Optim 54:361–373
- Su S (2010) Numerical approaches on shape optimization of elliptic eigenvalue problems and shape study of human brains. Diss. The Ohio State University
- Svanberg K (1987) The method of moving asymptotes—a new method for structural optimization. Int J Numer Methods Eng 24:359–373
- Wang C, Komodakis N, Paragios N (2013) Markov random field modeling, inference & learning in computer vision & image understanding: a survey. Computer Vision & Image Understanding 117:1610–1627
- Wang Y, Chen F, Wang MY (2017) Concurrent design with connectable graded microstructures. Comput Methods Appl Mech Eng 317:84– 101. https://doi.org/10.1016/j.cma.2016.12.007
- Wang Y, Luo Z, Zhang N, Kang Z (2014) Topological shape optimization of microstructural metamaterials using a level set method. Comput Mater Sci 87:178–186
- Wu Z, Xia L, Wang S, Shi T (2019) Topology optimization of hierarchical lattice structures with substructuring. Comput Methods Appl Mech Eng 345:602–617
- Xia L, Breitkopf P (2015) Design of materials using topology optimization and energy-based homogenization approach in Matlab. Struct Multidiscip Optim 52:1229–1241
- Yan X, Huang X, Zha Y, Xie YM (2014) Concurrent topology optimization of structures and their composite microstructures. Comput Struct 133:103–110
- Yu X, Ji Z, Liang H, Jiang Z, Wu L (2017) Mechanical metamaterials associated with stiffness, rigidity and compressibility: a brief review. Prog Mater Sci 94:S0079642517301445
- Zheludev NI (2010) The road ahead for metamaterials. Science 328:582–583
 Zhou S, Li Q (2008) Design of graded two-phase microstructures for tailored elasticity gradients. J Mater Sci 43:5157–5167. https://doi.org/10.1007/s10853-008-2722-y

Publisher's note Springer Nature remains neutral with regard to jurisdictional claims in published maps and institutional affiliations.

